Volume 1 | Number 1 | Jan 2013 | Pages 1–100

# Nanoscale

www.rsc.org/nanoscale

ROYAL SOCIETY
OF CHEMISTRY

This is an *Accepted Manuscript*, which has been through the Royal Society of Chemistry peer review process and has been accepted for publication.

*Accepted Manuscripts* are published online shortly after acceptance, before technical editing, formatting and proof reading. Using this free service, authors can make their results available to the community, in citable form, before we publish the edited article. We will replace this *Accepted Manuscript* with the edited and formatted *Advance Article* as soon as it is available.

You can find more information about *Accepted Manuscripts* in the **Information for Authors**.

Please note that technical editing may introduce minor changes to the text and/or graphics, which may alter content. The journal's standard **Terms & Conditions** and the **Ethical guidelines** still apply. In no event shall the Royal Society of Chemistry be held responsible for any errors or omissions in this *Accepted Manuscript* or any consequences arising from the use of any information it contains.

ROYAL SOCIETY
OF CHEMISTRY

www.rsc.org/nanoscale

# Journal Name

**ARTICLE**

## Substoichiometric Two-Dimensional Molybdenum Oxide Flakes: A Plasmonic Gas Sensing Platform

Manal M. Y. A. Alsaif,*[a] Matthew R. Field,[b] Billy J. Murdoch,[b] Torben Daeneke,[a] Kay Latham,[c] Adam F. Chrimes,[a] Ahmad Sabirin Zoolfakar,[a] Salvy P. Russo,[c] Jian Zhen Ou*[a] and Kourosh Kalantar-zadeh*[a]

**Abstract**

Two-dimensional (2D) molybdenum oxides at their various stoichiometries are emerging candidates for generating plasmon resonances in visible light range. Here, we demonstrate plasmonic 2D molybdenum oxide flakes for gas sensing applications in which hydrogen ($H_2$) is selected as a model gas. The 2D molybdenum oxide flakes are obtained using a grinding-assisted liquid exfoliation method and exposed to simulated sun to acquire its substoichiometric quasi-metallic form. After the exposure to $H_2$ gas molecules, the quasi-metallic molybdenum oxide flakes are partly transformed into semiconducting states, gradually losing their plasmonic properties. The novel 2D plasmonic sensing platform is tested using different concentrations of $H_2$ gas at various operating temperatures to comprehensively assess its sensing performance. The presented 2D plasmonic system offers great opportunities for future sensing and optical applications.

## 1. Introduction

Two-dimensional (2D) materials, which are made of single or few fundamental layers, have received increasing attention in recent years, owing to their unique electronic and optical properties.[1-3] The recent demonstrations of plasmon resonances in such 2D materials have shown several advantages over the conventional noble metal plasmonic systems.[3-8] One of the major challenges faced by such metals is that their plasmonic features cannot be significantly modulated as their free charge carrier concentrations are rather permanently locked.[3, 9, 10] In addition, noble metals are plagued with significant optical losses arising from their large Drude relaxation rates.[3,

[11] This limits their implementation in most of the optical communication applications, in which long wave propagation is needed.[3, 11]

Graphene plasmonics, which is a core member in the 2D plasmonics family, can be a viable solution to address the aforementioned challenges due to the ability to modulate its plasmonic properties by chemical, electrochemical and electrical approaches.[3, 5, 7] In particular, graphene can be doped with electron concentrations ranging from $\sim 10^{12}$ to $\sim 10^{14}$ cm$^{-2}$, corresponding to plasmon resonance positioned within far-infrared (FIR) and terahertz wavelengths.[12-14] Furthermore, the existence of massless electrons in graphene can greatly reduce its damping loss, resulting in significantly prolonged plasmon lifetime.[12, 15-17] However, such observations could not be extended to shorter wavelength regions, which are more viable for optical instrument industries, due to their insufficient carrier densities and other intrinsic properties.[18] Obtaining plasmon resonances in the near infrared (NIR) and visible regions is an importance goal for the development of future sensing and plasmonic data processing units, as these wavelengths are commonly used in standard optical systems.[19]

The creation of stable tuneable 2D plasmonic materials in the visible and NIR ranges is possible. We previously demonstrated that 2D quasi-metallic molybdenum oxide flakes generate strong visible plasmon resonance, which can be tuned by solar energy.[19] Such plasmonic tunability can be mainly ascribed to a combination of the possibility of high level ionic intercalation (hence ultra-doping capability) and the 2D geometrical effect on the plasmon dispersion.[19, 20] These 2D flakes were also implemented in an optical biosensing system model, where their plasmonic features were altered in the presence of bovine serum albumin (BSA), which started at a concentration as low as $\sim 0.15$ mg mL$^{-1}$.[19] These initial results have strongly encourage the future development of 2D plasmonic sensors that operate in common optical wavelengths and possibly

realise the capability of single molecular detection, owing to their ultra-sensitive plasmon inducing regions generated near the surface.[21-23]

2D molybdenum oxide is a stratified material with strong in-plane bonds and weak van der Waals forces coupling between layers,[1, 24-26] which provides plenty of room to accommodate ionic dopants not only from a liquid phase but also gaseous phase.[27] In addition, the surface of the 2D material shows strong affinity to certain gas molecules, in which the gas molecules can either be physisorbed or chemisorbed resulting in the change of its electronic and optical properties.[27] Another potential use of 2D material is the development of highly sensitive optical gas sensors.[5, 28, 29] It has been demonstrated that the field of plasmonic gas sensors is an important area for future research in optical devices, which can possibly lead to the development of sensors for various gas species including $H_2$, CO and $NO_2$ [29-34] with superior sensitivity and fast response and recovery kinetics.[35]

In this paper, for the first time we incorporate 2D molybdenum oxide flakes to develop a highly sensitive plasmonic gas sensing platform. $H_2$ is selected as a model gas for such investigations. The novel 2D plasmonic sensor is tested using different concentrations of $H_2$ gas at both room and elevated temperatures in the visible wavelengths ranging between 400 and 750 nm. The density functional theory (DFT) calculations and electron energy-loss spectroscopy (EELS) measurements along with Mie-Gans theory assessments are used as evidences for the existence of plasmon resonances. The operating principle of the 2D plasmonic sensor toward $H_2$ gas is subsequently proposed with the assistance of X-ray photoelectron spectroscopy (XPS) and Raman spectroscopy.

## 2. Experimental section

### 2.1 The synthesis of 2D molybdenum oxide flakes and fabrication of the plasmonic $H_2$ gas sensors

3 g of molybdenum trioxide ($MoO_3$) powder (99% purity, from China Rare Metal Material Co.) was ground with 0.6 ml acetonitrile for 30 min. The powder was then dispersed in a 50 vol % ethanol/water mixture (45 ml), subjected to probe-sonication (Ultrasonic Processor GEX500) for 120 min at 125 W, and then centrifuged at 6000 rpm for 30 min at room temperature. The yellow/blue supernatant containing high concentrations of 2D $MoO_3$ flakes was collected and transferred into small containers with 3 ml volume each. The supernatant was irradiated under the sun simulator (Abet Technologies LS-150) at the power of 100 mW $cm^{-2}$ for 5 h and subsequently drop-casted onto quartz substrates with the area of $10 \times 10$ $mm^2$ at a fixed amount of 100 μL. Subsequently the films were dried at 40 °C to allow water and ethanol residues to evaporate and form a rigid film for optical $H_2$ gas sensing. A catalytic layer (50 wt.% Au and 50 wt.% Pd) with the thickness of ~1 nm was sputtered onto the film surface to enhance the breakdown of $H_2$ gas molecules.

### 2.2 Characterisation of 2D molybdenum oxide flakes and their $H_2$ gas sensing performances

Bruker Multimode 8 atomic force microscopy (AFM) was used for analysing the surface topography. The Raman spectra measurements were performed using a CRAIC 20/30 PV microspectrophotometer with Raman capability (785 nm laser at the power of 100 mW). The dynamic light scattering (DLS) analysis was obtained using an ALV 5022F spectroscope. The X-ray diffraction (XRD) patterns were collected using a Bruker D4 ENDEAVOR. The XPS was performed using a Thermo Scientific K-alpha instrument with an Al Kα source. The scanning electron microscope (SEM) images were obtained using an FEI Nova NanoSEM. The 2D molybdenum oxide flakes supernatant sample (after 5 h solar light irradiation), were

dropped onto Cu grids for high-resolution transmission electron microscopy (HRTEM-JEOL 2100F) characterisation. HRTEM images were acquired using a Gatan Orius SC1000 CCD Camera. To conduct EELS experiments, a high-angle annular dark field (HAADF)-scanning transmission electron microscopy (STEM) image of the region of interest was first obtained. Then, a small area map was acquired across the nanoflakes and the total number of data points was determined such that one spectrum was collected at every 2 nm interval. The zero loss peak (ZLP) of each spectrum was aligned using Digital Micrograph and removed using the reflected tail model. Spin-dependent hybrid DFT calculations were performed using Gaussian basis set *ab initio* package CRYSTAL09.[36] A hybrid exchange-correlation functional was used based on the PBE0 model with the Hartree-Fock to density functional exchange ratio set to 0.2. [37] The Mo basis set used a Hay-Wadt type effective core pseudopotential to account for the core Mo electrons ($1s^2 2s^2 2p^6 3s^2 3p^6 3d^{10}$) and a 311-31G basis set for the valance electrons. This basis set was previously used by Cora *et. al*. to study $\alpha$-MoO$_3$.[38] For an oxygen atom, all electrons 8-411d1 basis set was used as previously by Cora.[39] The initial structures for $\alpha$-MoO$_3$[40], monoclinic Mo$_4$O$_{11}$[41] and monoclinic MoO$_2$ [42] were obtained from the published literature and then geometry-optimised using CRYSTAL09. The forces on all atoms after optimisation were less than 18 meV/A.

The absorbance spectrum of the films made of 2D molybdenum oxide nanoflakes was examined using a spectrophotometric system consisting of a Micropack DH-2000 UV-Vis-NIR single beam light source and an Ocean Optics HR4000 spectrophotometer, in which a blank quartz substrate was used as a reference.

Gas measurements were performed in a customised gas testing chamber with a temperature control (Fig. S1). A mass flow controlled gas calibration system was used for mixing dry synthetic air with different range of concentrations (600-10,000 ppm) of H$_2$ gas, and this gas was purged into the chamber at a regulated gas flow of 200 sccm.

## 3. Results and discussion

The plasmonic 2D molybdenum oxide flakes are synthesised using a method we have previously developed (details are presented in the experimental section).[19] In brief, 2D $MoO_3$ flakes are firstly obtained from the bulk $MoO_3$ powder using a grinding-assisted liquid exfoliation method. Subsequently, they are reduced to 2D molybdenum oxide ($MoO_{3-x}$) under the illumination of simulated solar light, in which the reduction degree depends on the illumination duration. The lateral dimensions of these suspended flakes are assessed using a DLS system (Fig. 1a). It is observed that these 2D flakes with dark blue colour mainly have lateral dimensions of ~100 nm after 5 h solar light illumination. Their thicknesses are found to be typically around 4 nm based on the AFM imaging (an example is shown in Fig. 1b). In addition, the crystal structure of these 2D flakes is investigated using XRD measurements. According to Fig. 1c, it is found that the illuminated 2D flakes exhibit a dominant crystal phase of monoclinic $Mo_4O_{11}$ with the lattice parameters of $a$ = 24.540 Å, $b$ = 5.439 Å, $c$ = 6.701 Å, and lattice angle: $\beta$ = 94.280° (JCPDs no: 13-0142). The XRD peaks appeared at 13.3, 26.2, 33, 36.7 and 46.2° 2θ, corresponding to the (0 0 1), (4 1 1), (0 2 0), (10 0 0), and (4 2 2) planes, respectively. High resolution transmission electron microscopy (HRTEM) is utilised to further confirm the crystal structure of 2D flakes (Fig. 1d). It is observed that lattice fringe spacing of 0.34 nm, can be indexed to the (4 1 1) plane of monoclinic $Mo_4O_{11}$. The extended Raman spectrum of the $Mo_4O_{11}$ film that is dried at 40 °C (Fig. S2a) reveals that there is no distinguished peak appearing beyond 1000 $cm^{-1}$, which indicates that the organic residue in the film can be neglected.[43, 44] In addition, the surface adhesion property of the flakes is revealed by the AFM with adhesion mapping capability (Fig. S2b). The adhesion mapping image in Fig.S2 shows that the flakes have similar surface energies.[45] The flakes are mostly placed horizontally on the substrate and on top of each other. As a result, the van der

Waals forces hold these flakes into a firm film with a good stability. The crude scratch test also confirms that the films have a reasonable adhesion to the surface of the substrate. The surface morphology of the film made of 2D molybdenum oxide flakes can also be seen in Fig. S3.
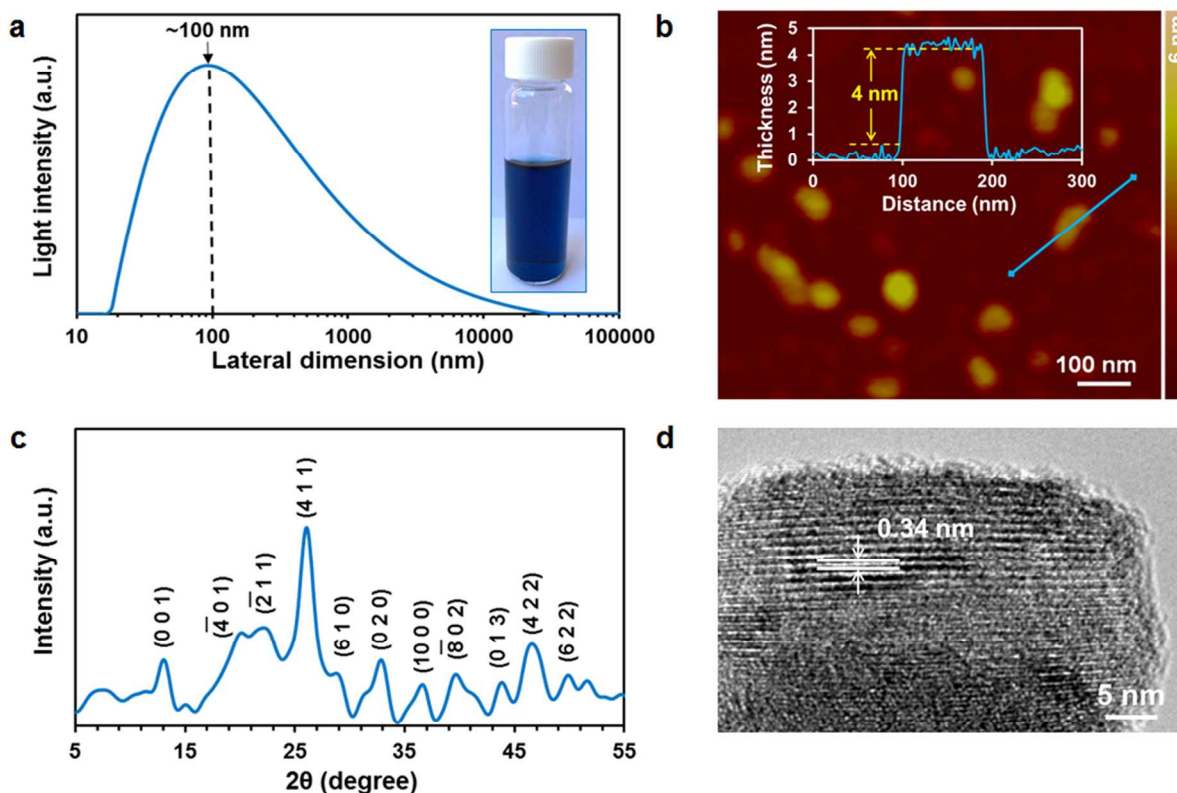


**Fig. 1.** (a) The DLS graph of 2D molybdenum oxide flakes after 5 h of solar light irradiation. The inset shows an optical image of suspended flakes. (b−d) The AFM image, the XRD pattern and the HRTEM image of 2D flakes, respectively.

DFT calculations are carried out firstly to elucidate the transition from 2D $\alpha$-$MoO_3$ to monoclinic $Mo_4O_{11}$ (detail of the calculation methods is presented in the Experimental section). As can be seen in Fig. 2a, a sharp peak is observed in the valence band edge centred at 5.4 eV for the semiconducting $\alpha$-$MoO_3$ and its

bandgap is calculated to be ~3.2 eV, which matches well with the literature.[46] Interestingly, the peak initially positioned in the valence band at 5.4 eV becomes less noticeable for $Mo_4O_{11}$. Instead, a small broad peak appears at 2.5 eV as shown in Fig. 2b. More importantly, $Mo_4O_{11}$ is found to be metallic with occupied bands corresponding to Mo and O across the Fermi-level due to the presence of a large number of oxygen vacancies. Such a semiconductor-metal transition suggests the generation of additional free electrons in the material, which can potentially produce collective excitations hence forming plasmons.
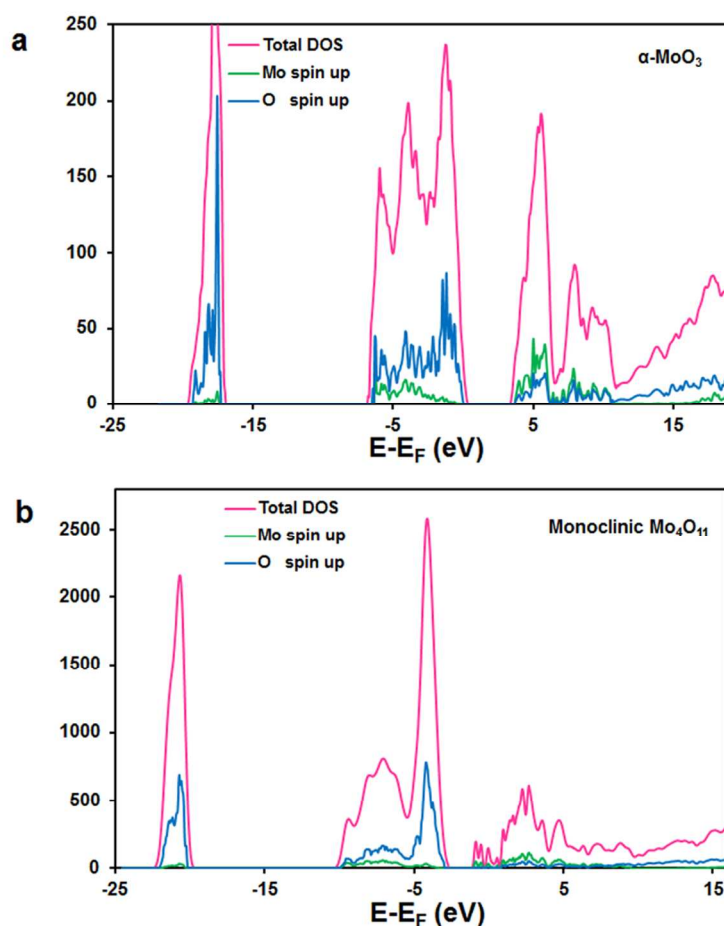


**Fig. 2** The density of states calculated by DFT of: (a) $\alpha$-$MoO_3$ and (b) Monoclinic $Mo_4O_{11}$.

The generation of plasmons is also confirmed by EELS in Fig.3.[47, 48] Fig. 3a shows the EELS spectrum collected from a 2D α-MoO$_3$ flake. Gaussian peak fitting technique is utilised to extract the plasmon and the interband transition modes from the spectrum. The deconvoluted peak at 5.4 eV can be ascribed to the interband transition.[49] Prominent peaks at 12.2 19, 23 eV are also observed, which can correspond to the plasmon modes induced by valence electrons in different composite outer atomic cells.[50] A broad peak at 36.2 eV can be assigned to the core-loss transition.[49] For the quasi-metallic Mo$_4$O$_{11}$ (Fig. 3b), an additional broad peak appearing at 49.6 eV can be ascribed to the core-loss transition resulting from Mo-4p excitation.[49, 51] More importantly, a strong peak also appears at 7.5 eV, which can be attributed to the additional plasmon mode originated by the generated free electron in the presence of oxygen vacancies.

This can be further validated by the theoretical calculation on bulk plasmon energy in the free electron gas model:

$$E_P = \hbar\omega_\mathrm{p} = \hbar\sqrt{\frac{Ne^2}{\varepsilon_0 m_e}} \qquad (1)$$

where $\hbar$ is the reduced Planck constant; the charge carrier density ( $N$ ) for Mo$_4$O$_{11}$ is ~8.5 × 10$^{21}$ cm$^{-3}$ as suggested by Alsaif et al.;[19] $\varepsilon_0$ is the permittivity of free space; and the effective mass of an electron is $m_e= 0.2m_o$.[52]

The calculated bulk plasmon energy is 7.6 eV, which well agrees with the EELS measurements. The surface plasmon energy in the 2D system is then obtained based on the calculated extinction coefficients using the Mie-Gans theoretical model, which is given by [53]:

$$A \, \alpha \, \omega\varepsilon_m^{\frac{3}{2}} \sum_j \frac{\left[\frac{1}{\mathrm{p_j}^2}\right]\varepsilon_2}{\left[\varepsilon_1 + \frac{1 - \mathrm{p_j}}{\mathrm{p_j}}\varepsilon_m\right]^2 + {\varepsilon_2}^2} \qquad (2)$$

where $\omega$ is the angular frequency of incident light; $\varepsilon_m$ is the dielectric constant of the medium, $\varepsilon_1$ and $\varepsilon_2$ are the real and imaginary terms of the dielectric function $\varepsilon(\omega)$ of the suspended material, respectively, and $p_j$ is the depolarisation factors for different axis (a = length, b = thickness and c = width). The depolarisation factors for a two-dimensional (2D) material are [19]:

$$P_b = \frac{1}{g^2}\left[1 - \left(\frac{1-g^2}{g^2}\right)^{\frac{1}{2}} \sin^{-1} g\right] \qquad (3)$$

$$P_a = P_c = \frac{1 - P_b}{2} \qquad (4)$$

in which the $g$ factor is:

$$g = \left(\frac{a^2 - b^2}{a^2}\right)^{1/2} \qquad (5)$$

Parameters for the 2D calculations are based on the DLS and AFM results shown in Fig. 1. Aspect ratio in 2D system is defined as the length over thickness. The lateral dimensions are considered to be equal in the 2D system. According to the results, $P_b$ is equal to $\sim 0.933$ while $P_a$ and $P_c$ are both equal to $\sim 0.033$. The dielectric function is described by:

$$\varepsilon(\omega) = \varepsilon_1 + i\varepsilon_2 = \varepsilon_\infty - \frac{\omega_p^2}{\omega^2 + i\gamma\omega} \qquad (6)$$

in which $\omega_p$ is the bulk plasmon frequency, $\varepsilon_\infty$ is the high-frequency relative dielectric constant which is equal to 20 and $\gamma$ is the damping coefficient of the resonance as:

$$\gamma = \frac{1}{\tau} = \frac{e^2}{\sigma m_e} \qquad (7)$$

where $\tau$ is the scattering time of an electron and the conductivity ($\sigma$) is $2 \times 10^3 \, \Omega^{-1} \, cm^{-1}$.[19]

The theoretical values of the surface plasmon resonances of the quasi-metallic $Mo_4O_{11}$ are ~730 nm, which corresponds to the surface plasmon energy of ~1.7 eV. Although the surface plasmon cannot be observed by the EELS spectrum due to it being within the zero loss peak, it matches well with the position of the optical absorption peak centred at 750 nm as shown in Fig. 4a, hence suggesting the this absorption peak can be attributed to the surface plasmon resonance.
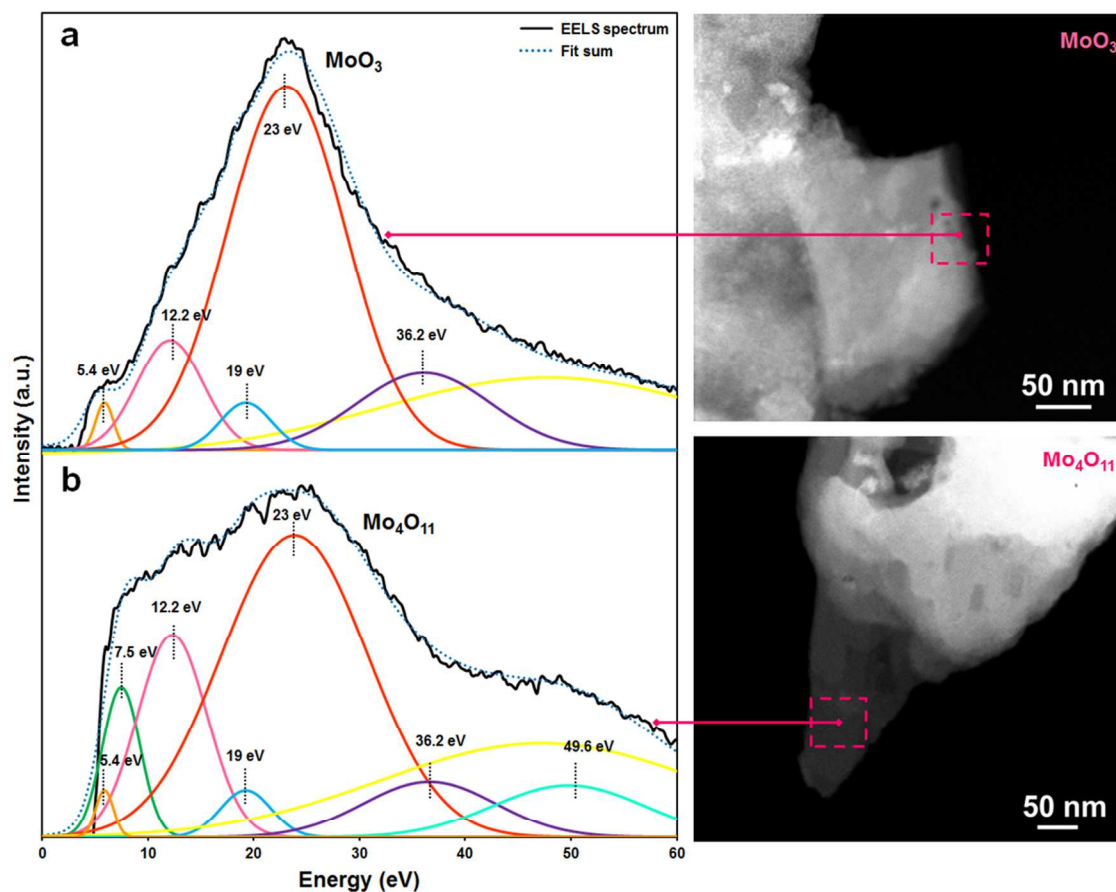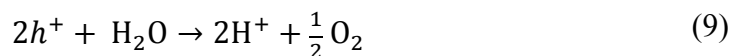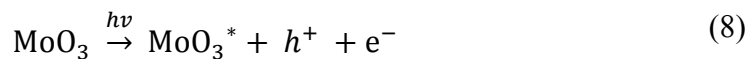


**Fig. 3** (a) EELS spectrum of 2D α-$MoO_3$ mapped to the corresponding STEM image to the right. (b) EELS spectrum of the quasi-metallic 2D $Mo_4O_{11}$ mapped to the corresponding STEM image to the right. These graphs show the two extracted spectra with plural scattering (multiple plasmon resonances) removed, which eliminates the thickness effects.

The plasmonic $H_2$ gas sensors are fabricated by drop-casting a fixed amount of the suspended 2D flakes onto quartz substrates (details are found in the Experimental section). Subsequently, these samples are sputtered with an Au/Pd catalytic layer (thickness of ~1 nm) for facilitating the breakdown of $H_2$ gas molecules.[27] These sensors are firstly placed into a customized design chamber, which consists of an aluminium box with quartz windows (Fig. S1). They are then exposed to synthetic air containing a range of different concentrations (600-10,000 ppm) of $H_2$ gas, at operating temperatures ranging from 20 to 100 °C. The optical absorption features of the sensors are measured *in situ* upon various gas exposure stages. The light intensity of the optical source is measured to be ~1 mW cm$^{-2}$ at 550 nm. At such weak optical power intensity, no crystal phase change is observed for the films even after hours of exposure to the light in ambient air or at elevated temperatures. This is evident by the XRD measurement (Fig. S4) that presented no change in the peaks after light exposure four hours and is also confirmed by the baseline repeatability during the gas sensing tests (it is shown in the later sections). Fig. 4a shows the optical absorption property of the film made of 2D molybdenum oxide flakes before the exposure to $H_2$ gas at 20 °C (room temperature). The broad absorption peak centred at ~750 nm is ascribed to the plasmon resonance feature of 2D $Mo_4O_{11}$ flakes as being confirmed by the EELS experiments (Fig. 3) and Mie-Gans theoretical calculations.

After being exposed to 10,000 ppm of $H_2$ gas concentration for 20 min, this plasmonic absorption peak is further broadened and the absorbance value is slightly increased. Such a change is generally associated with the loss of metallic properties of the material under investigation. We have previously conducted XPS measurements and Raman spectroscopy to show that a portion of the quasi-metallic 2D $Mo_4O_{11}$ flakes is transformed into semiconducting 2D $MoO_2$, even in the solar stimulation reduction process of 2D $MoO_3$. This is due to the interaction with $H^+$ ions, which are formed from water splitting.[19] Water-

splitting occurs when the oxide suspensions are irradiated with solar light, as the result, electrons and holes are generated.[54, 55] The intercalation process can be expressed as follows[19, 56, 57]:

$$MoO_3 \xrightarrow{h\nu} MoO_3{}^* + h^+ + e^- \tag{8}$$

$$2h^+ + H_2O \rightarrow 2H^+ + \tfrac{1}{2}O_2 \tag{9}$$

$$MoO_3 + xH^+ + xe^- \rightarrow H_x MoO_3 \tag{10}$$

Under the high power solar light irradiation, $H_x MoO_3$ will eventually be transformed into $MoO_{3-x}$ ($Mo_4O_{11}$ in this case).[19, 58] Here, $H_2$ gas molecules are broken into $H^+$ ions, producing the 2D $MoO_2$ flakes in a similar manner. $MoO_2$ is a semiconductor with a relatively narrow band gap of ~1.6 eV. The DFT calculations of α-$MoO_3$, Monoclinic $Mo_4O_{11}$ and Monoclinic $MoO_2$ are shown in Fig. S5a-c. It is interesting that a strong peak can be observed in the region between −1 to across 0 eV for $MoO_2$ (Fig. S5c), which is possibly due to the generated free electrons, occupying part of the d bands of the oxide.[59] Therefore, visible plasmon resonance features is gradually lost during the transition from $Mo_4O_{11}$ to $MoO_2$.

The alteration of the $Mo_4O_{11}$ stoichiometry, and the consequent loss of plasmon resonance feature, can be explained using the "hydrogen spill-over model".[27, 60, 61] The Au/Pd layer assists with the dissociation of $H_2$ gas molecules into electrons and $H^+$ ions.[62, 63] The $H^+$ ions are then intercalated into the $Mo_4O_{11}$ crystal structure, forming OH or $OH_2$ groups together with the lattice O atoms. This eventually causes the further reduction of $Mo_4O_{11}$ into a more thermodynamically stable phase of $MoO_2$ and simultaneously generating water molecules. This is evident by the change of absorption features, also confirmed by XPS analysis and Raman spectroscopy, which are shown in later sections. Such a process can be expressed as follows:

$$Mo_4O_{11} + 6H^+ + 6e^- \rightarrow 4MoO_2 + 3H_2O \qquad (11)$$

When the film is exposed to air again, the $O^{2-}$ ions, which are generated by the dissociation of $O_2$ on the Au/Pd layer, transferred to the $MoO_2$ crystal structure and recombined with a number of oxygen vacancies, transforming the 2D flakes back to $Mo_4O_{11}$.[58, 63] However, the accumulation of water molecules on the $MoO_2$ surface may reduce the available surface catalytic sites for the dissociation of $O_2$, although the incoming dry air stream encourages only a portion of the water molecules to desorb from the surface. Therefore, this can explain the incomplete recovery of the initial crystal phase, especially at room temperature. Alternatively, the interlayer diffusion rate of O atoms in $MoO_2$ is much slower than that of $H^+$ ions, which could also be a contributing factor to the slow air recovery process.

As the transformation from $Mo_4O_{11}$ to $MoO_2$ results in the alteration of optical absorption features over the whole visible light region,[64] sensors dynamic response (absorbance change with the respect of time in seconds) is investigated for different optical wavelengths ranged from 400 to 750 nm towards different concentrations of $H_2$ gas (600-10,000 ppm) as shown in Fig. 4b. It is found that the baselines for the sensors dynamic response are drifted at all measured wavelengths as the poor sensor recovery occurs at the $H_2$ gas concentration as low as 600 ppm at room temperature.
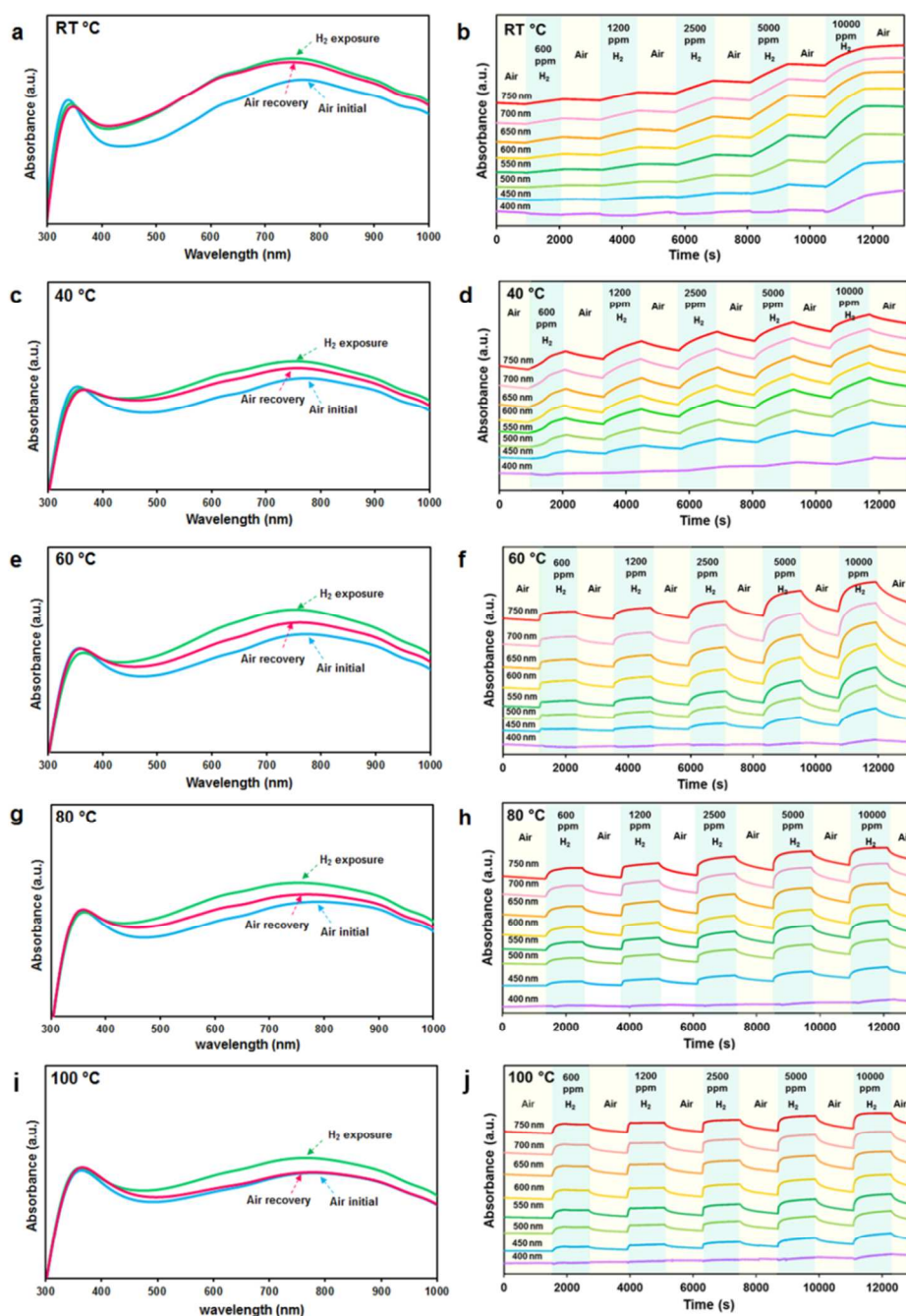
**Fig. 4** (a, c, e, g, i) The UV-Vis spectra of the 2D molybdenum oxide flakes before and after 10,000 ppm of $H_2$ gas exposure as well as the subsequent recovery in air. (b, d, f, h, j) The dynamic responses for different wavelengths of (400−750 nm) towards different concentrations of $H_2$ gas (600-10,000 ppm) at operating temperatures of 20 (room temperature−RT), 40, 60, 80 and 100 °C.

When the operating temperature is increased from 20 to 40 °C and above up to 100 °C (operation above 100 °C is not possible as the test chamber could not stand higher temperatures), it is observed that the initial absorption peak ascribing the 2D $Mo_4O_{11}$ plasmon resonance gradually flattens (Fig. 4c,e,g,i). As the XPS and Raman spectroscopy results suggest (which will be shown later), when the film is exposed to air at elevated temperatures, a part of 2D $Mo_4O_{11}$ is oxidised and transformed into low stoichiometry and eventually the fully-stoichiometric 2D $MoO_3$. This result occurred in two simultaneous reactions during the exposure to 10,000 ppm of $H_2$ gas concentration: the oxidising by-products are reduced back to $Mo_4O_{11}$, while the residual $Mo_4O_{11}$ is further reduced to $MoO_2$. This is evident by their smaller variation of absorption features compared to that at room temperature operation after the $H_2$ gas exposure. Moreover, there is an improvement in the recovery of the sample's plasmonic features at elevated temperatures (Fig. 4c,e,g,i), indicating the heat energy facilitates the water molecule desorption from the surface.[62, 63] The best operating temperature is found to be at 100 °C for the plasmon absorbance peak of $Mo_4O_{11}$ towards 10,000 ppm of $H_2$ gas concentration, in which it shows a considerable response magnitude and recovers back to the initial state after being exposed to air (Fig. 4i). This indicates that increasing the sample temperature to 100 °C enhances the rate of oxygen vacancy recombination, making it comparable with the rate of oxygen vacancy formation.[63]

While the sensor response is not fully recovered for all $H_2$ gas concentration at 40 °C (Fig. 4d), there is an obvious enhancement in the dynamic response associated with stability of response baselines when increasing the temperature from 60 to 100 °C (Fig. 4f,h,j). Such elevated temperatures can be used for overcoming the thermodynamic barrier, effectively allowing faster adsorption/desorption of ions onto the plasmonic film.[62] These elevated temperatures also likely assist in the formation and evaporation of the $H_2O$ molecules in the process, helping to improve

the dynamics of the reactions. The best dynamic response, with a stable baseline, is observed at 100 °C (Fig. 4j), in which the gas interaction reaches equilibrium at such a temperature. The response and recovery time of the sensors are defined as the duration needed for the devices to undergo an absorbance change from 10% to 90% and from the no $H_2$ gas exposure to fully exposed condition. Alternatively, the response time ($t_{90}$) and recovery time ($t_{10}$) are defined as the time required for the sensor output to reach 90% of the full-scale value (maximum absorbance peak) and drop to 10% of the full-scale value (maximum absorbance peak) respectively.[27] The response factor in a percentage is defined as the ratio of the optical absorbance change of the plasmonic film over that in air and can be described by as follows:

$$RF = ((Abs_{air} - Abs_{gas})/Abs_{air}) \times 100\% \tag{12}$$

Fig. 5a shows the dynamic response of plasmonic 2D molybdenum oxide towards 10,000 ppm of $H_2$ gas concentration at wavelength of 750 nm for different operating temperatures from 20 to 100 °C. The particular wavelength of 750 nm is chosen because it represents the centre of the broad absorption peak of quasi-metallic 2D $Mo_4O_{11}$. It is found that the recovery time of the plasmonic molybdenum oxide film after exposure to the air was slower at room temperature than at elevated temperatures (Fig. 5b). The largest response factor at wavelength of 750 nm is found to be 20 % for operating temperatures of 60 °C, while the lowest is found to be 4.4 % at 20 °C. The response factor of the sensors depends on the operating temperatures.[27] The data in Table 1 are extracted from Fig. 5a-b, which summarises the response factor and the response and recovery time of plasmonic sensor at wavelength of 750 nm.
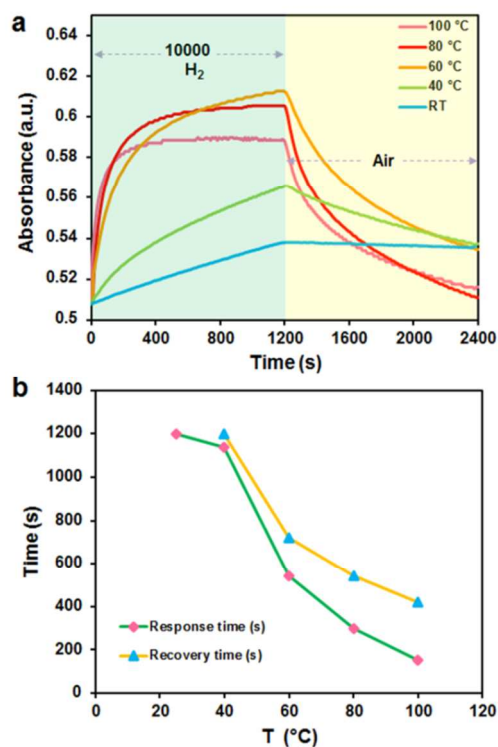
**Fig. 5** (a) The absorbance values of $Mo_4O_{11}$ plasmonic peak over time at the wavelength of 750 nm associated with operating temperatures of 20, 40, 60, 80 and 100 °C at different gas exposure stages. (b) The corresponding response and recovery time at different operating temperatures.

**Table 1.** The summary of the sensor response factor as well as response and recovery time at different operating temperatures.

| Operating temperature | Response factor | Response time | Recovery time |
|:---:|:---:|:---:|:---:|
| (°C) | (%) | (s) | (s) |
| 20 | 4.4 | 1200 | N/A |
| 40 | 10.2 | 1140 | 1200 |
| 60 | 20 | 540 | 720 |
| 80 | 18.3 | 300 | 540 |
| 100 | 15.7 | 150 | 420 |

The H$_2$ gas responses of the 2D molybdenum oxide films of different thicknesses are investigated. These different thicknesses are obtained by drop-casting various volumes (50, 100, 250 and 500 µL) of the suspension solution onto quartz substrates. These result in film thicknesses of approximately 650 nm, 1 µm, 1.35 µm and 1.65 µm, respectively. The samples are tested towards 10,000 ppm of H$_2$ gas while their temperatures are hold at the optimum value of 100 °C. It can be seen in Fig. 6a-d, while response and recovery time are the shortest for the 650 nm sample, the response magnitude is very small in comparison to the other thicknesses (Fig. 6e-h), which is not directly compared with others. Therefore it is observed that the sample made of the 1 µm film shows the best recovery to the baseline and stability.
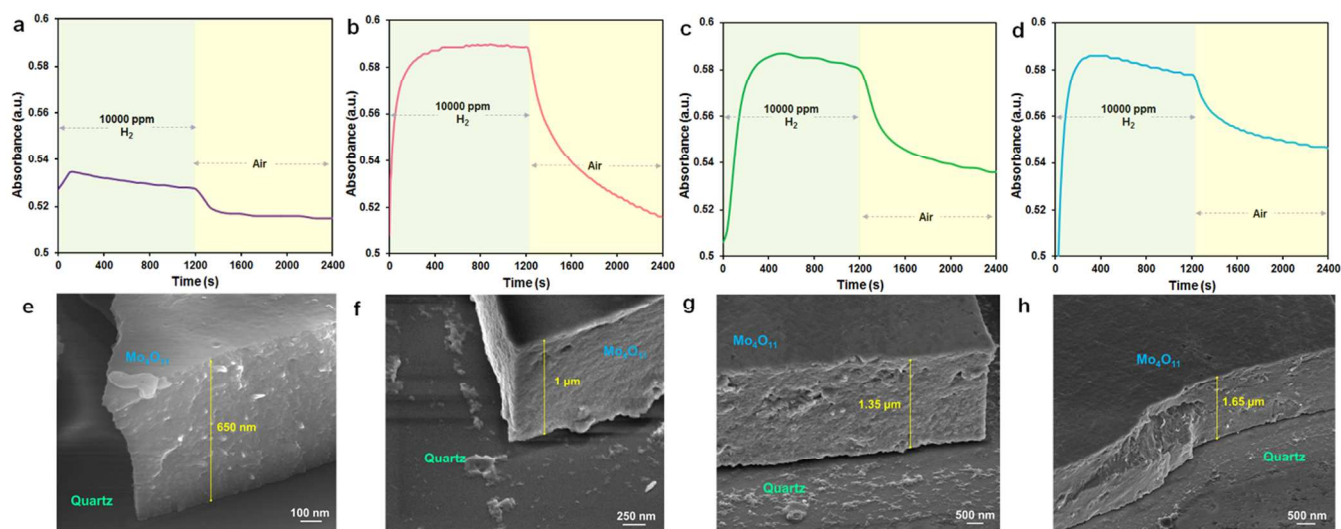


**Fig. 6.** (a-d) The plasmonic peak (750 nm) absorbance values of 2D molybdenum oxide films of different thicknesses over time towards 10,000 ppm of H$_2$ gas at the operating temperature of 100 °C. (e-h) The SEM images of samples with different film thicknesses of 650 nm, 1 µm, 1.35 µm and 1.65 µm, respectively.

XPS measurements are carried out to investigate the stoichiometry of the films after exposure to 10,000 ppm of $H_2$ gas concentration at various operating temperatures. From Fig. 7a, the initial sample is presented to have a complex mixture of Mo $3d_{5/2,3/2}$ spin doublets of molybdenum in its oxidation state of +4, +5, and +6.[65] Two moderate peaks centred at 229.3 and 232.4 eV can be attributed to the bonding energies of Mo $3d_{5/2}$ and Mo $3d_{3/2}$ orbital electrons of $Mo^{4+}$, respectively, suggesting the presence of a significant amount of $MoO_2$.[66-68] Relatively stronger doublet peaks centred at 230.1 eV for $Mo^{5+}$ $3d_{5/2}$ and 233.2 eV for $Mo^{5+}$ $3d_{3/2}$ are also detected, indicating the presence of $Mo_4O_{11}$ as the dominant phase.[69] However, a lowermost doublet centred at 232.2 eV and 235.3 eV, representing the characteristics of fully-stoichiometric $MoO_3$, can be attributed for higher oxidation states of $Mo^{6+}$ $3d_{5/2}$ and $Mo^{6+}$ $3d_{3/2}$, respectively.[67, 69] This might be due to a slight oxidation introduced into the sample during preparation process.[19]
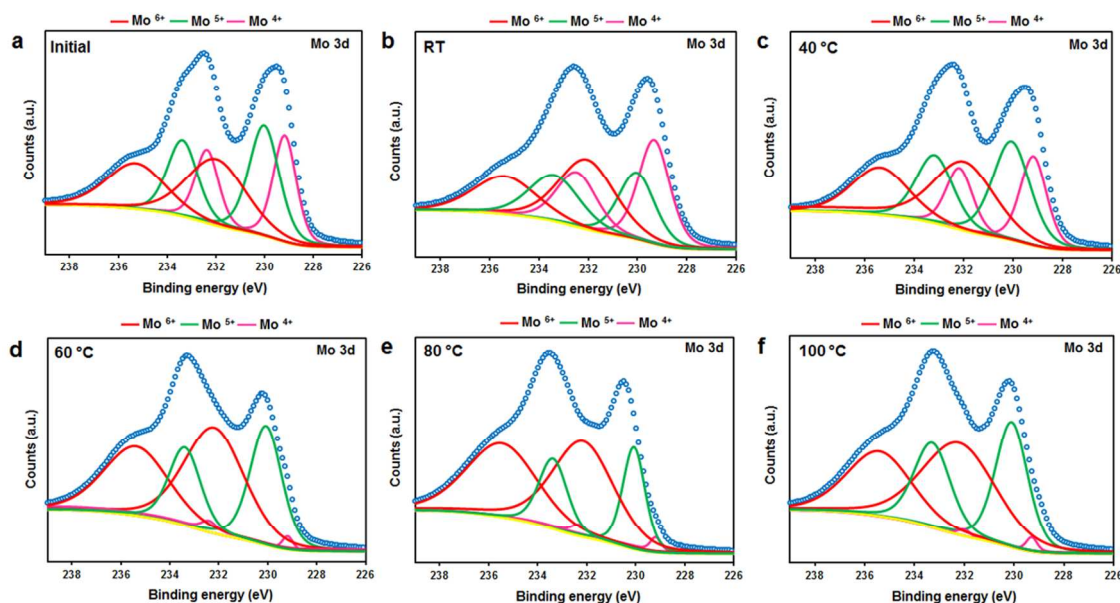


**Fig. 7** XPS spectrum of Mo 3d for 2D quasi-metallic molybdenum oxide flakes before and after exposure to 10,000 ppm of $H_2$ gas concentration at different operating temperatures.

When the sample is exposed to $H_2$ gas at 20 °C (Fig. 7b), the peaks at lower oxidation state ($Mo^{4+}$) increase whereas, the peaks at oxidation state ($Mo^{5+}$) slightly decrease due to the increase of the content of oxygen vacancies.[67, 70, 71] Increasing the operating temperatures upon the exposure to 10,000 ppm of $H_2$ gas concentration results in the augmentation of both $Mo^{5+}$ and $Mo^{6+}$ oxidation state peaks and the peaks at lower oxidation state ($Mo^{4+}$) decrease (Fig. 5c,d,e,f).[67] This can be attributed to the "two simultaneous reactions" mechanism that we described previously, in which transformation of $MoO_3$ to $Mo_4O_{11}$ (+6 to +5 oxidation state) and $Mo_4O_{11}$ to $MoO_2$ (+5 to +4 oxidation state) occur at the same time. When the operating temperature is above 60 °C, only a small signature of $MoO_2$ is observed, indicating that the transformation of $MoO_3$ to $Mo_4O_{11}$ (+6 to +5 oxidation state) dominates the "two simultaneous reactions" process.[65, 66, 72]

In addition to the XPS analysis, the research investigated the Raman spectra of the 2D plasmonic samples after the exposure to 10,000 ppm of $H_2$ gas concentration at various operating temperatures to further validate the proposed reaction model (Fig. 8). It is found that the Raman peaks are observed at 342, 657, 818 and 964 $cm^{-1}$ for the initial sample, which are all in good agreement with a combination of monoclinic $Mo_4O_{11}$.[73-75] The strong peak that occurs at 964 $cm^{-1}$ can be assigned to the stretching vibration of terminal oxygen atoms $v(O=Mo)$; and the peak at 818 $cm^{-1}$ is assigned to the stretching mode of doubly coordinated oxygen atoms $v(O-Mo_2)$. In addition, the peak that occurs at 657 $cm^{-1}$ is attributed to the stretching mode of triply coordinated oxygen atoms $v(O-Mo_3)$, and the peak at 342 $cm^{-1}$ is assigned to the deformation mode of triply coordinated oxygen atoms $\delta(O-Mo_3)$.[67, 70, 75, 76] In addition, the peaks at 230, 472 and 724 $cm^{-1}$ are assigned to monoclinic $MoO_2$.[75] There is no distinguishable difference between the Raman spectra before and after $H_2$ concentration of 10,000 ppm exposure at an operating temperature lower than 40 °C.[67] However, at the operating temperatures above 60 °C, the intensity of all

$Mo_4O_{11}$ and $MoO_2$ Raman peaks are gradually reduced, again confirming that the oxidation process significantly interrupts the $H_2$ gas reduction process at these temperatures.[58, 62, 72, 77]
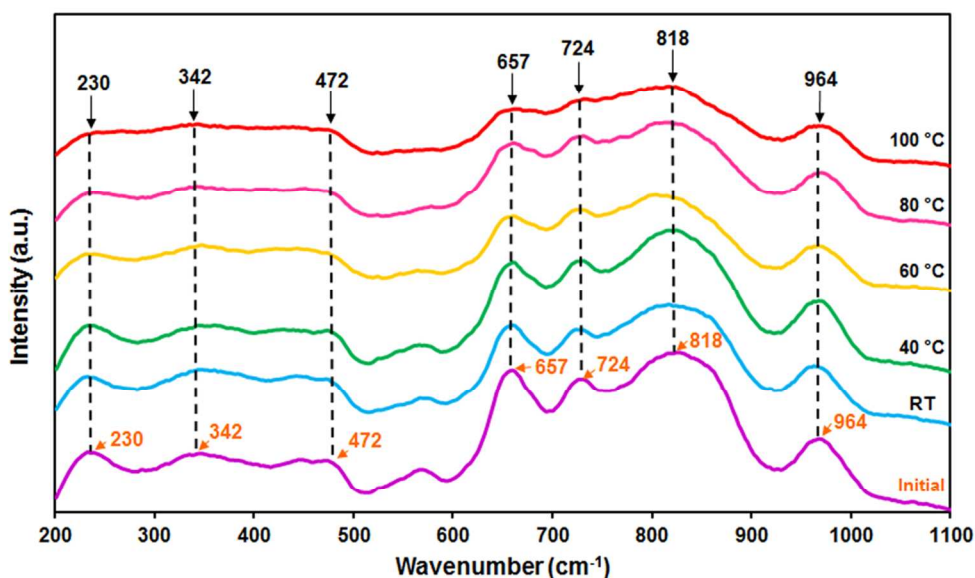


**Fig. 8** The Raman spectrum of 2D molybdenum oxide films before and after exposure to 10,000 ppm of $H_2$ gas concentration at different operating temperatures of 20 (room temperature – RT), 40, 60, 80 and 100°C.

The plasmonic sensor described in this work show an optimum response factor of ~20% at 60 °C and a relatively short response and recovery time of 150 and 420 s, respectively, at 100 °C. A comparison with previous plasmonic $H_2$ gas sensors is presented in Table S1. Qadri *et al.* demonstrated a response factor of 0.16% towards 10,000 ppm of $H_2$ gas concentration which is less efficient than the one demonstrated in this work.[78] Additionally, Cittadini *et al.* presented a response factor of ~ 0.4% towards 10,000 ppm of $H_2$ gas concentration with a response/recovery time in several minute ranges,[79] while our sensors showed a better optical response performance than this work. In another report by Ohodnicki Jr. *et al.*, the response factor was 33% at 500 °C in the NIR range,[32] while our sensor shows a more stable response at low

temperatures in the visible range. Although, Dharmalingam *et al.* reported the highest optical response factor of 150%, this response was obtained at a relatively high operating temperature of 500 °C.[30] It should be emphasised that our films made of substoichiometric 2D molybdenum oxide flakes are operated at a relatively low operating temperature of 100 °C.

## 4. Conclusions

Quasi-metallic 2D molybdenum oxide flakes were utilised as a sensitive material for plasmonic $H_2$ gas sensing applications. The plasmonic sensors were tested at room and elevated temperatures of up to 100 °C towards $H_2$ concentration of 10,000 ppm in the visible light range. After the exposure to $H_2$ gas at room temperature, the plasmonic absorption peak of the flakes was broadened and the absorbance value was slightly increased, suggesting that a portion of quasi-metallic $Mo_4O_{11}$ was transformed into semiconducting $MoO_2$. However at elevated temperatures, the plasmonic absorption peak was gradually flattened, which suggest two simultaneous reactions mechanism occurred at the same time that were the transformation of $MoO_3$ to $Mo_4O_{11}$ and $Mo_4O_{11}$ to $MoO_2$. In addition, the dynamic response towards different concentrations of $H_2$ gas (600-10,000 ppm) in synthetic air were investigated for different optical wavelengths ranged from 400 to 750 nm. The best wavelength for the dynamic response towards different concentrations of $H_2$ gas was at 750 nm. The 2D plasmonic sensor showed the highest response factor of 20% at 60 °C and shortest response/recovery time at 100 °C. The XPS and Raman spectra analysis confirmed two simultaneous chemical reactions mechanisms, consistent with the plasmonic $H_2$ gas sensing results. These results suggest that sensors based on 2D quasi-metallic molybdenum oxide flakes lead to altered plasmon dispersion relationships, which provide opportunities to create high performance 2D optical systems in the future.

       *J. Name.*, 2012, **00**, 1-3 | **23**

## Acknowledgements

## Notes and references

[a] School of Electrical and Computer Engineering, RMIT University, Melbourne, Victoria, Australia. *E-mail:S3372431@student.rmit.edu.au, jianzhen.ou@rmit.edu.au and Kourosh.kalantar@rmit.edu.au.

[b] RMIT Microscopy and Microanalysis Facility, RMIT University, Melbourne, Victoria, Australia.

[c] School of Applied Sciences, RMIT University, Melbourne, Victoria, Australia.

† Electronic supplementary information (ESI) available: Details on optical gas measurement setup and theoretical plasmon resonance peak calculations. See DOI: 10.1039/b000000x/

## References

1 Q. H. Wang, K. Kalantar-Zadeh, A. Kis, J. N. Coleman and M. S. Strano, *Nat. Nanotechnol.*, 2012, **7**, 699-712.

2 S. Balendhran, S. Walia, H. Nili, J. Z. Ou, S. Zhuiykov, R. B. Kaner, S. Sriram, M. Bhaskaran

and K. Kalantar-zadeh, *Adv. Funct. Mater.*, 2013, **23**, 3952-3970.

3 G. V. Naik, V. M. Shalaev and A. Boltasseva, *Adv. Mater.*, 2013, **25**, 3264-3294.

4 J. J. Cha, K. J. Koski, K. C. Y. Huang, K. X. Wan, W. Luo, D. Kong, Z. Yu, S. Fan, M. L. Brongersma and Y. Cui, *Nano Lett.*, 2013, **13**, 5913-5918.

5 A. N. Grigorenko, M. Polini and K. S. Novoselov, *Nat. Photonics*, 2012, **6**, 749-758.

6 P. Cudazzo, M. Gatti and A. Rubio, *New J. Phys.*, 2013, **15**, 125005.

7 Z. Fei, A. S. Rodin, G. O. Andreev, W. Bao, A. S. McLeod, M. Wagner, L. M. Zhang, Z. Zhao, M. Thiemens, G. Dominguez, M. M. Fogler, A. H. C. Neto, C. N. Lau, F. Keilmann and D. N. Basov, *Nature*, 2012, **487**, 82-85.

8 G. Eda and S. A. Maier, *ACS Nano*, 2013, **7**, 5660-5665.

9 D. A. Bobb, G. Zhu, M. Mayy, A. V. Gavrilenko, P. Mead, V. I. Gavrilenko and M. A. Noginov, *Appl. Phys. Lett.*, 2009, **95**, 151102

10 K. F. MacDonald, Z. L. Samson, M. I. Stockman and N. I. Zheludev, *Nat. Photonics*, 2009, **3**, 55-58.

11 P. R. West, S. Ishii, G. V. Naik, N. K. Emani, V. M. Shalaev and A. Boltasseva, *Laser Photonics Rev.*, 2010, **4**, 795-808.

12 M. Jablan, M. Soljacic and H. Buljan, *Phys. Rev. B*, 2014, **89**, 085415.

13 C. Si, W. Duan, Z. Liu and F. Liu, *Appl. Phys. Lett.*, 2012, **109**, 226802.

14 H. Medina, Y.-C. Lin, D. Obergfell and P.-W. Chiu, *Adv. Funct. Mater.*, 2011, **21**, 2687-2692.

15 K. S. Novoselov, A. K. Geim, S. V. Morozov, D. Jiang, Y. Zhang, S. V. Dubonos, I. V. Grigorieva and A. A. Firsov, *Science*, 2004, **306**, 666-669.

16 K. S. Novoselov, A. K. Geim, S. V. Morozov, D. Jiang, M. I. Katsnelson, I. V. Grigorieva, S. V. Dubonos and A. A. Firsov, *Nature*, 2005, **438**, 197-200.
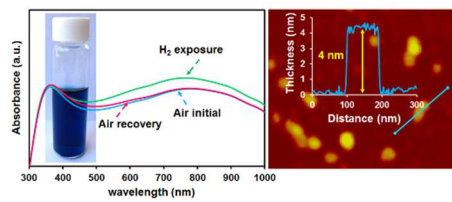
17 M. Jablan, M. Soljacic and H. Buljan, *Proc. IEEE*, 2013, **101**, 1689-1704.

**Nanoscale Accepted Manuscript**

18 L. Ju, B. Geng, J. Horng, C. Girit, M. Martin, Z. Hao, H. A. Bechtel, X. Liang, A. Zettl, Y. R. Shen and F. Wang, *Nat. Nanotechnol.*, 2011, **6**, 630-634.

19 M. M. Y. A. Alsaif, K. Latham, M. R. Field, D. D. Yao, N. V. Medehkar, G. A. Beane, R. B. Kaner, S. P. Russo, J. Z. Ou and K. Kalantar-zadeh, *Adv. Mater.*, 2014, **26**, 3931-3937.

20 X. Liu and M. T. Swihart, *Chem. Soc. Rev.*, 2014, **43**, 3908-3920.

21 A. Tittl, P. Mai, R. Taubert, D. Dregely, N. Liu and H. Giessen, *Nano Letters*, 2011, **11**, 4366-4369.

22 P. Zijlstra, P. M. R. Paulo and M. Orrit, *Nat. Nanotechnol.*, 2012, **7**, 379-382.

23 S. K. Mishra and B. D. Gupta, *Plasmonics*, 2012, **7**, 627-632.

24 K. S. Novoselov, D. Jiang, F. Schedin, T. J. Booth, V. V. Khotkevich, S. V. Morozov and A. K. Geim, *Proc. Natl. Acad. Sci. U. S. A.*, 2005, **102**, 10451-10453.

25 D. Hanlon, C. Backes, T. M. Higgins, M. Hughes, A. O'Neill, P. King, N. McEvoy, G. S. Duesberg, B. M. Sanchez, H. Pettersson, V. Nicolosi and J. N. Coleman, *Chem. Mater.*, 2014, **26**, 1751-1763.

26 Z. Y. Wang, S. Madhavi and X. W. Lou, *J. Phys. Chem. C*, 2012, **116**, 12508-12513.

27 M. M. Y. A. Alsaif, S. Balendhran, M. R. Field, K. Latham, W. Wlodarski, J. Z. Ou and K. Kalantar-zadeh, *Sens. Actuators, B*, 2014, **192**, 196-204.

28 T. Daisuke, S. Shuhei, U. Eiji, W. Pangpang, O. Koichi and T. Kaoru, *Jpn. J. Appl. Phys.*, 2014, **53**, 01AF01.

29 W. C. Tan, M. Hofmann, Y.-P. Hsieh, M. L. Lu and Y. F. Chen, *Nano Res.*, 2012, **5**, 695-702.

30 G. Dharmalingam, N. A. Joy, B. Grisafe and M. A. Carpenter, *Beilstein J. Nanotechnol.*, 2012, **3**, 712-721.

31 S.-B. Wang, Y.-F. Huang, S. Chattopadhyay, S. J. Chang, R.-S. Chen, C.-W. Chong, M.-S. Hu, L.-C. Chen and K.-H. Chen, *NPG Asia Mater.*, 2013, **5**, e49.

Nanoscale Accepted Manuscript

32 P. R. Ohodnicki Jr., C. Wang and M. Andio, *Thin Solid Films*, 2013, **539**, 327-336.

33 N. A. Joy, B. K. Janiszewski, S. Novak, T. W. Johnson, S.-H. Oh, A. Raghunathan, J. Hartley and M. A. Carpenter, *J. Phys. Chem. C*, 2013, **117**, 11718-11724.

34 N. Liu, M. L. Tang, M. Hentschel, H. Giessen and A. P. Alivisatos, *Nat. Mater.*, 2011, **10**, 631-636.

35 B. Chadwick, J. Tann, M. Brungs and M. Gal, *Sens. Actuators, B*, 1994, **17**, 215-220.

36 R. Dovesi, R. Orlando, B. Civalleri, C. Roetti, V. R. Saunders and C. M. Zicovich-Wilson, *Z. Kristall.*, 2005, **220**, 571-573.

37 C. Adamo and V. Barone, *J. Chem. Phys.*, 1999, **110**, 6158-6170.

38 F. Cora, A. Patel, N. M. Harrison, C. Roetti and C. Richard A. Catlow, *J. Mater. Chem.* , 1997, **7**, 959-967.

39 F. Cora, *Mol. Phys.*, 2005, **103**, 2483-2496.

40 H. Negishi, S. Negishi, Y. Kuroiwa, N. Sato and S. Aoyagi, *Phys. Rev. B*, 2004, **69**.

41 M. Ghedira, H. Vincent, M. Marezio, J. Marcus and G. Furcaudot, *J. Solid State Chem.*, 1985, **56**, 66-73.

42 D. E. Cox, R. J. Cava, D. B. McWhan and D. W. Murphy, *J. Phys. Chem. Solids*, 1982, **43**, 657-666.

43 V. Lemos and F. Camargo, *J. Raman Spectrosc.*, 1990, **21**, 123-126.

44 T. E. Coldea, C. Socaciu, F. Fetea, F. Ranga, R. M. Pop and M. Florea, *Not. Bot. Horti Agrobot. Cluj-Napoca*, 2013, **41**, 143-149.

45 A. S. Zoolfakar, R. A. Rani, A. J. Morfa, S. Balendhran, A. P. O'Mullane, S. Zhuiykov and K. Kalantar-zadeh, *J. Mater. Chem.*, 2012, **22**, 21767-21775.

46 D. Xiang, C. Han, J. Zhang and W. Chen, *Sci. Rep.*, 2014, **4**.

47 A. L. Koh, K. Bao, I. Khan, W. E. Smith, G. Kothleitner, P. Nordlander, S. A. Maier and D.

**Nanoscale Accepted Manuscript**

W. McComb, *ACS Nano*, 2009, **3**, 3015-3022.

48 J. A. Scholl, A. L. Koh and J. A. Dionne, *Nature*, 2012, **483**, 421-U468.

49 L. Lajaunie, F. Boucher, R. Dessapt and P. Moreau, *Phys. Rev. B*, 2013, **88**.

50 K. Iakoubovskii, K. Mitsuishi, Y. Nakayama and K. Furuya, *Phys. Rev. B*, 2008, **77**.

51 V. J. Keast, *J. Electron Spectrosc. Relat. Phenom.*, 2005, **143**, 97-104.

52 S. Balendhran, J. Deng, J. Z. Ou, S. Walia, J. Scott, J. Tang, K. L. Wang, M. R. Field, S. Russo, S. Zhuiykov, M. S. Strano, N. Medhekar, S. Sriram, M. Bhaskaran and K. Kalantar-zadeh, *Adv. Mater.*, 2013, **25**, 109-114.

53 G. C. Papavassiliou, *Solid State Chem*, 1979, **12**, 185-271.

54 R. Abe, K. Shinmei, N. Koumura, K. Hara and B. Ohtani, *J. Am. Chem. Soc.*, 2013, **135**, 16872-16884.

55 R. Abe, K. Sayama, K. Domen and H. Arakawa, *Chem. Phys. Lett.*, 2001, **344**, 339-344.

56 L. Zheng, Y. Xu, D. Jin and Y. Xie, *Chem. Mater.*, 2009, **21**, 5681-5690.

57 F. E. Osterloh, *Chem. Mater.*, 2008, **20**, 35-54.

58 J. Z. Ou, J. L. Carnpbell, D. Yao, W. Wlodarski and K. Kalantar-zadeh, *J. Phys. Chem. C* 2011, **115**, 10757-10763.

59 M. T. Greiner and Z.-H. Lu, *NPG Asia Mater.*, 2013, **5**.

60 J. G. Kim and J. R. Regalbuto, *J. Catal.*, 1993, **139**, 175-190.

61 B. Liu, D. Cai, Y. Liu, D. Wang, L. Wang, Y. Wang, H. Li, Q. Li and T. Wang, *Sens. Actuators, B*, 2014, **193**, 28-34.

62 J. Z. Ou, M. H. Yaacob, M. Breedon, H. D. Zheng, J. L. Campbell, K. Latham, J. du Plessis, W. Wlodarski and K. Kalantar-zadeh, *Phys. Chem. Chem. Phys.*, 2011, **13**, 7330-7339.

63 M. H. Yaacob, M. Breedon, K. Kalantar-zadeh and W. Wlodarski, *Sens. Actuators, B*, 2009, **137**, 115-120.

**Nanoscale Accepted Manuscript**

64 T. Matsushima and C. Adachi, *J. Appl. Phys.*, 2008, **103**, 034501.

65 V. Bhosle, A. Tiwari and J. Narayan, *J. Appl. Phys.*, 2005, **97**, 083539.

66 B. Brox and I. Olefjord, *Surf. Interface Anal.*, 1988, **13**, 3-6.

67 M. Vasilopoulou, A. M. Douvas, D. G. Georgiadou, L. C. Palilis, S. Kennou, L. Sygellou, A. Soultati, I. Kostis, G. Papadimitropoulos, D. Davazoglou and P. Argitis, *J. Am. Chem. Soc.*, 2012, **134**, 16178-16187.

68 F. Werfel and E. Minni, *J. Phys. C: Solid State Phys.*, 1983, **16**, 6091-6100.

69 J. Swiatowska-Mrowiecka, S. de Diesbach, V. Maurice, S. Zanna, L. Klein, E. Briand, I. Vickridge and P. Marcus, *J. Phys. Chem. C*, 2008, **112**, 11050-11058.

70 L. Seguin, M. Figlarz, R. Cavagnat and J. C. Lassegues, *Spectrochim. Acta, Part A*, 1995, **51**, 1323-1344.

71 J. G. Choi and L. T. Thompson, *Appl. Surf. Sci*, 1996, **93**, 143-149.

72 P. A. Spevack and N. S. McIntyre, *J. Phys. Chem.*, 1992, **96**, 9029-9035.

73 M. Dieterle, G. Weinberg and G. Mestl, *Phys. Chem. Chem. Phys.*, 2002, **4**, 812-821.

74 M. Dieterle and G. Mestl, *Phys. Chem. Chem. Phys.*, 2002, **4**, 822-826.

75 M. A. Camacho-Lopez, L. Escobar-Alarcon, M. Picquart, R. Arroyo, G. Cordoba and E. Haro-Poniatowski, *Opt. Mater.*, 2011, **33**, 480-484.

76 A. Phuruangrat, J. S. Chen, X. W. Lou, O. Yayapao, S. Thongtem and T. Thongtem, *Appl. Phys. A: Mater. Sci. Process.*, 2012, **107**, 249-254.

77 G. Mestl, P. Ruiz, B. Delmon and H. Knozinger, *J. Phys. Chem.*, 1994, **98**, 11269-11275.

78 M. U. Qadri, A. F. D. Diaz, M. Cittadini, A. Martucci, M. C. Pujol, J. Ferre-Borrull, E. Llobet, M. Aguilo and F. Diaz, *Sensors* 2014, **14**, 11427-11443.

79 M. Cittadini, M. Bersani, F. Perrozzi, L. Ottaviano, W. Wlodarski and A. Martucci, *Carbon*, 2014, **69**, 452-459.

Nanoscale Accepted Manuscript

TOC Figure